JGR Oceans

RESEARCH ARTICLE

10.1029/2025JC022927

Key Points:

- A one-dimensional analytical tidal wave model was developed, considering water storage and longitudinal currents over intertidal areas
- Intertidal zones modulate tides by increasing the wavenumber, depending on the relative importance of inertia, convergence, and friction
- Longitudinal currents over intertidal areas partly counterbalance the overall effects of intertidal areas by decreasing the wavenumber

Supporting Information:

Supporting Information may be found in the online version of this article.

Correspondence to:

X. Wei,
xwei@noc.ac.uk

Citation:

Zhu, R., Zhang, W., & Wei, X. (2026). Impact of intertidal areas on tidal propagation in tidally dominated estuaries. Part I: Theoretical formulation. *Journal of Geophysical Research: Oceans*, *131*, e2025JC022927. https://doi.org/10.1029/2025JC022927

Received 26 MAY 2025
Accepted 11 JAN 2026

Author Contributions:

Conceptualization: Renjie Zhu, Wei Zhang, Xiaoyan Wei
Formal analysis: Renjie Zhu
Funding acquisition: Renjie Zhu, Wei Zhang, Xiaoyan Wei
Investigation: Renjie Zhu, Xiaoyan Wei
Methodology: Renjie Zhu, Xiaoyan Wei
Project administration: Wei Zhang, Xiaoyan Wei
Software: Renjie Zhu, Xiaoyan Wei
Supervision: Wei Zhang, Xiaoyan Wei
Validation: Renjie Zhu
Visualization: Renjie Zhu, Xiaoyan Wei
Writing – original draft: Renjie Zhu, Xiaoyan Wei
Writing – review & editing: Renjie Zhu, Wei Zhang, Xiaoyan Wei

Impact of Intertidal Areas on Tidal Propagation in Tidally Dominated Estuaries. Part I: Theoretical Formulation

Renjie Zhu[1,2,3,4], **Wei Zhang**[1,2,3], **and Xiaoyan Wei**[4]

[1]State Key Laboratory of Water Disaster Prevention, Hohai University, Nanjing, China, [2]Key Laboratory of Ministry of Education for Coastal Disaster and Protection, Hohai University, Nanjing, China, [3]College of Harbour, Coastal and Offshore Engineering, Hohai University, Nanjing, China, [4]National Oceanography Centre, Liverpool, UK

Abstract Intertidal zones, such as saltmarshes and mudflats, face significant pressure from climate change and human activities, threatening the sustainable functioning of estuarine ecosystems. Using a one-dimensional analytical model that resolves the coupled tidal motions in the channel and intertidal areas, we systematically investigated the impact of intertidal zones on tidal propagation in tidally dominated estuaries. Unlike previous analytical studies considering only the effect of water storage over intertidal areas (IWS), our model resolves both IWS and the water exchange between the channel and intertidal areas due to longitudinal currents over intertidal areas (ILC). Our analytical solution demonstrates intertidal zones increase the complex tidal wavenumber (k) through the width and water flux ratios between the intertidal and channel regions, representing the IWS and ILC effects, respectively. The effects of intertidal areas on k depend on the relative importance of local inertia, width convergence, and bottom friction. In weakly dissipative, weakly convergent estuaries, increases in k induced by intertidal zones bring estuaries closer to resonance when the real part of kL (with L the estuary length) is below its resonance threshold (amplifying tides) and move them further from resonance when above (damping tides). In strongly dissipative, weakly/moderately convergent estuaries, intertidal areas consistently cause tidal damping by increasing k. In weakly/moderately dissipative, strongly convergent estuaries, tides are hardly influenced by intertidal zones. The ILC effect reduces k, thereby partly counteracting the aforementioned overall effects of intertidal areas. A comprehensive sensitivity analysis of the ILC process is conducted in Part II of this study.

Plain Language Summary Intertidal areas like mudflats and saltmarshes are vital parts of estuaries but are increasingly at risk due to climate change and human activity. These zones interact with tides in complex ways, affecting how tides propagate along estuaries. In this study, we developed a simplified mathematical model to understand how intertidal areas influence tidal behavior. Unlike earlier models, ours includes both the water storage and longitudinal flow over intertidal zones. We found that intertidal areas can either amplify or dampen tides, depending on the local inertia acceleration, estuary width convergence, and bottom resistance. In some estuaries, intertidal zones can bring tides closer to a resonant state, making them stronger, while in others, they weaken tidal oscillations. Along-estuary currents over intertidal areas, however, tend to make opposite contributions to the total effects of intertidal areas on tidal propagation. These findings help explain how changes to intertidal zones, whether through natural processes or human alteration, can affect tidal dynamics and estuarine ecosystems.

1. Introduction

Estuarine intertidal zones, such as mudflats, sandflats, saltmarshes, and mangroves, are vital ecosystems in estuaries that experience cyclical exposure at low tide and submergence at high tide. These areas serve crucial functions by providing breeding and nursing grounds for marine species, mitigating global warming through carbon capture and storage, improving estuarine water quality by filtering pollutants, and safeguarding against flooding and erosion hazards by dissipating wave energy (Möller et al., 2014). Unfortunately, intertidal areas are rapidly diminishing worldwide due to coastal development and climate change (Murray et al., 2019). To mitigate the escalating risks of flooding, erosion, and biodiversity loss posed by climate change [e.g., sea-level rise, intensified extreme weather (Athanase et al., 2024)] and human activities [e.g., damming, dredging, and land reclamation (Talke & Jay, 2020)], efforts to conserve, restore, and create intertidal zones are increasingly pursued around the world as nature-based solutions (Moraes et al., 2022). Given the critical roles of tides in estuarine flooding, bed erosion, and the transport of waterborne materials (e.g., sediment, salt, nutrients, pollutants), it is crucial to understand how intertidal zones and their changes affect tidal motions in estuaries.

Numerical models have been widely used in exploring the effects of intertidal areas on estuarine tidal dynamics in subtidal regions. Considering an idealized estuary with a trapezoidal cross-section, Speer and Aubrey (1985) revealed that intertidal zones cause tidal damping in the channel, with the effect becoming more pronounced as the intertidal bed slope decreases or bed friction increases. Similarly, Zheng et al. (2003) reported that intertidal flats dampen the principal tide in the Satilla River estuary (US), and Stark et al. (2017) found that incorporating intertidal storage basins causes tidal damping along the Scheldt estuary (Netherlands). In contrast, Oey et al. (2007) observed that intertidal zones result in a ∼20% increase in the tidal range in the upper region of Cook Inlet (US), while L. Li et al. (2012) found that intertidal areas enhance the principal tide in Darwin Harbour (Australia). These studies show that the impact of intertidal zones on tidal propagation can vary significantly from estuary to estuary, highlighting the need for a systematic understanding of how intertidal areas affect tidal propagation across different estuaries.

In comparison to the high computational cost of numerical models and the complexity of their results, idealized analytical or semi-analytical models are computationally cheaper and more effective for understanding the contributions of different processes that control the effects of intertidal areas on the estuarine tidal motion, as well as their sensitivity to changes in estuarine parameters (Schuttelaars et al., 2013). For this reason, idealized, cross-sectionally averaged analytical models have been used to systematically investigate the role of intertidal flats in estuarine tidal propagation and its dependence on estuary characteristics. Jay (1991) found that water storage over intertidal flats during flood phases slows down tide propagation in the channel with strong topography. Friedrichs and Madsen (1992) reported a more significant decay of the principal tidal wave in frictionally dominated embayments with a larger width ratio between the intertidal zone and the channel. Friedrichs and Aubrey (1994) highlighted the importance of intertidal areas to the generation of overtides in strongly convergent estuaries. Winterwerp and Wang (2013) found that intertidal areas slightly increase the tidal amplitude in small, narrow convergent estuaries with a large water depth. Hepkema et al. (2018) underscored the significance of momentum dissipation over intertidal flats in dampening tidal waves in the channel and the strong sensitivity of tidal characteristics to the flat-to-channel area ratio.

Nevertheless, all these analytical studies are based on the assumption of negligible currents (e.g., full momentum sink) over the intertidal area and only account for the effect of water storage over intertidal areas on the estuarine tidal dynamics. This assumption seems reasonable for estuaries with strong bed friction and weak longitudinal currents over intertidal areas (Jay, 1991). However, it may not be suitable for macro-tidal estuaries such as the Gomso, Ribble, Humber, and Seine estuaries, or meso-tidal systems like the Skagit River during spring tides, where intertidal zones can be wider than the channel (Cundy et al., 2007; J. Dronkers, 2016; Townend & Whitehead, 2003; van der Wal et al., 2002). Even though tidal currents over intertidal areas are weaker than currents in the channel, significant along-estuary flow velocities of up to 0.5–1 m/s have been observed within the intertidal area of such estuaries (Huang et al., 2022; Kim & Cho, 2017; Ralston et al., 2013; Verney et al., 2006; Wood et al., 1998).

Despite their potential importance, along-estuary currents over intertidal areas remain poorly monitored in most estuaries due to the technical challenges and high costs associated with conducting field measurements across vast intertidal areas. As a result, their role in estuarine tidal dynamics under various conditions remains unclear. This knowledge gap significantly limits our understanding of tidal propagation in estuaries with extensive intertidal areas, particularly as human activities and climate change continue to alter key estuarine and intertidal zone characteristics (e.g., length, width, bed elevation, bottom roughness) (C. Li et al., 2016; Talke & Jay, 2020). To understand the impact of intertidal areas on estuarine hydrodynamics, R. Zhu et al. (2025a) developed a three-dimensional (3D) semi-analytical model that dynamically couples the water motions in the intertidal and channel regions. They found that intertidal areas tend to amplify leading-order tides in shorter estuaries but significantly dampen them in longer ones, and these effects become weaker when stronger estuary width convergence or a narrower intertidal zone is considered. Nevertheless, their study is limited to a few specific sets of estuary parameters. The effect of intertidal areas on tidal propagation across a broader range of parameters (e.g., width, depth, friction, forcing) remains unexplored. More importantly, although their semi-analytical 3D model provides valuable insights into the effects of intertidal areas on the magnitude and horizontal/vertical structure of estuarine circulation, the numerical procedure involved prevents an analytical solution from being derived to understand

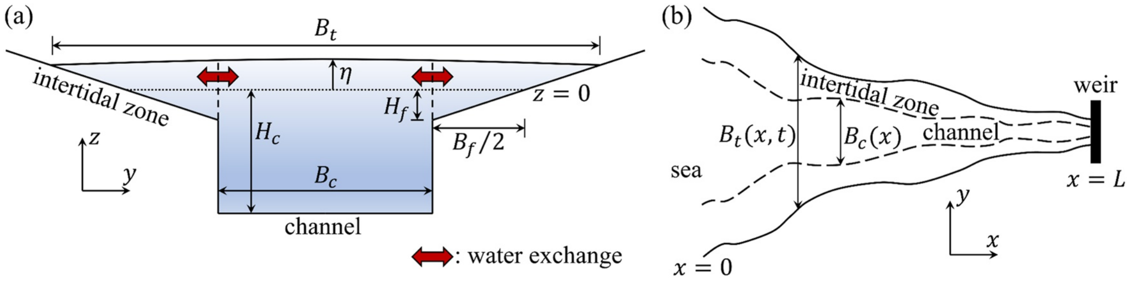

Figure 1. (a) The cross-sectional view and (b) top view of an idealized estuary. Here x, y, and z are the longitudinal, lateral, and vertical coordinates with t as time. The undisturbed water level is at $z = 0$ (dotted line). The free surface is located at $z = \eta$. The bottom is at $z = -h$, with $h = H_c$ in the channel and $h = H_f$ at the interface between the channel and intertidal zones (dashed lines). The seaward and landward boundaries are respectively at $x = 0$ (i.e., mouth) and $x = L$ (i.e., head), with L the estuary length. The channel width is denoted by B_c and the intertidal area width at $z = 0$ is denoted by B_f. The total width of the estuary including both the channel and the time-varying intertidal area is $B_t = B_c + \left(1 + \eta/H_f\right)B_f$.

the underlying mechanisms of how estuarine tidal propagation is affected by the individual contributions of different intertidal processes, such as longitudinal currents and water storage over intertidal areas.

To comprehend the role of intertidal areas in tidal dynamics in estuaries, in this study we develop a one-dimensional analytical model that considers both the water storage and longitudinal currents over intertidal areas, extending the model of Jay (1991). Our model considers idealized, tidally dominated (e.g., macro-tidal or meso-tidal during spring tides) estuaries with an exponentially converging width and a linear intertidal bed profile. We have two main goals in this study: (1) to derive an analytical solution for estuarine tidal wave propagation accounting for the effects of both water storage (IWS) and longitudinal currents (ILC) over intertidal areas; and (2) to reveal how intertidal areas influence tidal propagation through IWS and ILC across estuaries with different characteristics (e.g., length, width, depth, convergence, friction).

This paper, called Part I, is structured as follows: Section 2 describes the research methodology; Section 3 investigates the effects of intertidal areas on the complex tidal wavenumber and resonance together with the along-estuary patterns of tidal wave propagation; Section 4 discusses the implications and limitations of our study; conclusions are drawn in Section 5. The stage is set for the work in Part II, which systematically investigates how the strength of longitudinal currents over intertidal areas and the significance of ILC effects on tides respond to changes in estuary characteristics and forcing conditions.

2. Methodology

2.1. Model Description

Building upon the model of Jay (1991), our model considers an idealized estuary with a deep, flat-bed channel (consistently submerged) and triangular intertidal areas symmetrically distributed on each side (Figure 1a). In this model, the water motion in the channel and intertidal areas is described by two different systems of one-dimensional shallow water equations, which are derived by averaging the three-dimensional shallow water equations over the channel and intertidal cross-sections, respectively. These one-dimensional equations are dynamically coupled through the non-zero lateral water exchange (Figure 1a, red arrows) across the interface between the channel and intertidal zones (Figure 1b, dashed lines).

Utilizing the hydrostatic assumption and Boussinesq approximation (Cushman-Roisin & Beckers, 2011), the three-dimensional shallow water equations read:

$$\frac{\partial u}{\partial x} + \frac{\partial v}{\partial y} + \frac{\partial w}{\partial z} = 0. \tag{1a}$$

$$\frac{\partial u}{\partial t} + \nabla \cdot (u\mathbf{U}) = -g\frac{\partial \eta}{\partial x} + \frac{\partial}{\partial z}\left(A_v \frac{\partial u}{\partial z}\right), \tag{1b}$$

$$\frac{\partial v}{\partial t} + \nabla \cdot (v\mathbf{U}) = -g\frac{\partial \eta}{\partial y} + \frac{\partial}{\partial z}\left(A_v \frac{\partial v}{\partial z}\right), \tag{1c}$$

Here, g is the acceleration of gravity, A_v denotes the vertical eddy viscosity, and $\mathbf{U} = (u, v, w)$ is the velocity vector, with u, v, and w the flow velocity in the x, y, and z directions. In this study, the effects of Coriolis deflection, density gradients, and horizontal mixing are ignored for simplicity (see Text S1 in Supporting Information S1).

At the estuary mouth ($x = 0$), a periodically oscillating tidal forcing is prescribed:

$$\eta = a_m \cos(\sigma t). \tag{2a}$$

Here, σ denotes the tidal frequency, and a_m represents the tidal amplitude, which is laterally uniform at the mouth. This means the same tidal forcing is imposed in the channel and intertidal areas. A weir is located at the estuary head ($x = L$, see Figure 1b), where a constant river discharge Q is prescribed:

$$\int_{-\frac{B_t}{2}}^{\frac{B_t}{2}} \int_{-h}^{\eta} u \, dz \, dy = -Q. \tag{2b}$$

At the free surface ($z = \eta$), the kinematic and shear-free boundary conditions are applied:

$$w = \frac{\partial \eta}{\partial t} + \boldsymbol{u}_{\mathrm{h}} \cdot (\nabla \eta), \text{and } A_v \frac{\partial \boldsymbol{u}_{\mathrm{h}}}{\partial z} = (0, 0). \tag{2c}$$

At the bottom ($z = -h$), an impermeable condition and a partial-slip boundary condition are imposed:

$$w = -\boldsymbol{u}_{\mathrm{h}} \cdot (\nabla h), \text{and } A_v \frac{\partial \boldsymbol{u}_{\mathrm{h}}}{\partial z} = s \boldsymbol{u}_{\mathrm{h}}. \tag{2d}$$

Here, $\boldsymbol{u}_{\mathrm{h}} = (u, v)$ is the horizontal velocity vector, and s is the slip parameter by assuming linear bottom friction, which varies from zero in the free-slip condition to a large value in the no-slip condition (R. Zhu et al., 2025a). All key physical variables used in the model formulation are summarized in Table S1 of the Supporting Information S1.

2.1.1. Shallow Water Equations for the Channel

By averaging the three-dimensional shallow water equations (Equation 1) over the channel cross-section and applying the kinematic and dynamics vertical boundary conditions (Equations 2c and 2d), the system of one-dimensional water motion equations for the channel is derived (see Text S1 in Supporting Information S1):

$$\frac{\partial}{\partial x}\left[u_c B_c (H_c + \eta_c)\right] + B_c \frac{\partial \eta_c}{\partial t} + 2F_n = 0, \tag{3a}$$

$$\frac{\partial u_c}{\partial t} + u_c \frac{\partial u_c}{\partial x} + 2\,\frac{M_n - u_c F_n}{B_c (H_c + \eta_c)} = -g \frac{\partial \eta_c}{\partial x} - \frac{s_c}{H_c + \eta_c} u_c. \tag{3b}$$

Here, u_c and η_c are the cross-sectionally averaged longitudinal velocity and water level in the channel. The terms F_n and M_n represent the depth-integrated water and momentum exchange across the interface between the channel and intertidal zones, respectively:

$$F_n = \int_{-h}^{\eta} \boldsymbol{u}_{\mathrm{h}} \cdot \boldsymbol{n}_{\mathrm{h}} \, dz \bigg|_{y=\pm\frac{B_c}{2}}, \tag{4a}$$

$$M_n = \int_{-h}^{\eta} (\boldsymbol{u}_{\mathrm{h}} \cdot \boldsymbol{n}_{\mathrm{h}}) u \, dz \bigg|_{y=\pm\frac{B_c}{2}}, \tag{4b}$$

with $\boldsymbol{n}_{\mathrm{h}}$ the horizontal normal vector pointing outwards

$$\boldsymbol{n}_{\mathrm{h}} = \left(-\frac{1}{2}\frac{dB_c}{dx}, \pm 1\right)\Bigg|_{y=\pm\frac{B_c}{2}}. \tag{5}$$

The parameter s_c, derived from averaging the slip parameter s over the channel, is the linearized channel bottom friction coefficient, which measures the average strength of bottom friction within the channel. Equation 3 indicates that the effect of intertidal areas on tidal propagation in the channel is driven by the water and momentum exchange (i.e., F_n and M_n), although the latter only plays a secondary role in tidally dominated estuaries (see Section 2.2.1).

The seaward boundary ($x = 0$) condition in the channel is

$$\eta_c = a_m \cos(\sigma t), \tag{6a}$$

and the water flux across the channel Q_c (see Equation S6, Text S1 in Supporting Information S1) at the landward boundary ($x = L$) reads

$$Q_c = u_c B_c \left(H_c + \eta_c\right), \tag{6b}$$

which, plus the intertidal water flux Q_f, equals the river discharge Q (Equation 2b).

2.1.2. Shallow Water Equations for the Intertidal Zone

Likewise, the system of one-dimensional water motion equations for the intertidal area is derived by averaging the three-dimensional shallow water equations (Equation 1) over the intertidal cross-section [see Text S2 in Supporting Information S1, see also in R. Zhu et al. (2025a)]:

$$\frac{\partial}{\partial x}\left[u_f B_f \frac{\left(H_f + \eta_f\right)^2}{4H_f}\right] + B_f \frac{H_f + \eta_f}{2H_f}\frac{\partial \eta_f}{\partial t} - F_n = 0, \tag{7a}$$

$$\frac{\partial u_f}{\partial t} + u_f \frac{\partial u_f}{\partial x} - 4H_f \frac{M_n - u_f F_n}{B_f \left(H_f + \eta_f\right)^2} = -g\frac{\partial \eta_f}{\partial x} - \frac{2s_f}{H_f + \eta_f} u_f. \tag{7b}$$

Here, u_f and η_f are the intertidal cross-sectionally averaged longitudinal velocity and water level. The parameter s_f, derived from averaging the slip parameter s over the intertidal region, is the linearized bottom friction coefficient in the intertidal area, which measures the average strength of bottom friction over the intertidal zone.

The continuity equations (Equations 3a and 7a) account for the divergence of the longitudinal flow and the temporal variation of the water storage in the channel and intertidal areas, respectively, which are balanced by the lateral water exchange F_n. The lateral exchange term in the momentum equations, that is, the third term in Equations 3b and 7b driven by the contributions from F_n and M_n, are derived from the cross-sectional average of the three-dimensional advection term, that is, the second term in Equation 1b.

The seaward boundary condition in the intertidal area is

$$\eta_f = a_m \cos(\sigma t), \tag{8a}$$

and the water flux across the intertidal part of the landward boundary Q_f (see Equation S7, Text S1 in Supporting Information S1) reads

$$Q_f = u_f B_f \frac{\left(H_f + \eta_f\right)^2}{2H_f}, \tag{8b}$$

with

$$Q_c + Q_f = u_c B_c (H_c + \eta_c) + u_f B_f \frac{(H_f + \eta_f)^2}{2H_f} = -Q. \tag{8c}$$

So far, we have derived four governing equations (Equations 3a, 3b, 7a, and 7b) with six unknowns (i.e., $\eta_c, \eta_f, u_c, u_f, F_n$, and M_n). Since the momentum exchange (M_n) does not contribute to the principal tide (see Section 2.2), only one additional equation is needed to close the system of equations. Here, we assume the intertidal water level is equal to the channel water level at the same longitudinal location, that is, $\eta_c = \eta_f$.

2.1.3. Iterative Linearization Procedure of the Quadratic Bottom Stress

In this study, the bottom friction is linearized to derive analytical solutions. The original quadratic bottom shear stresses read

$$\tau_b^c = \rho C_d^c |u_c| u_c, \text{and } \tau_b^f = \rho C_d^f |u_f| u_f. \tag{9a}$$

Here, ρ is the water density, and τ_b^c and τ_b^f denote the bottom shear stresses in the channel and intertidal areas, respectively, with C_d^c and C_d^f the prescribed drag coefficients in two regions. The linear bottom shear stresses in the channel and the intertidal areas read

$$\tau_b^c = \rho s_c u_c, \text{and } \tau_b^f = \rho s_f u_f. \tag{9b}$$

Following Hepkema et al. (2018), the linearized bottom friction coefficients are determined by the Lorentz linearization condition: the energy dissipation within the channel and intertidal areas during a tidal cycle $T = 2\pi/\sigma$ remains the same when using either linearized or quadratic bottom shear stress formulations. This yields

$$\int_0^L \int_0^T B_c C_d^c |u_c| u_c^2 \, dt \, dx = \int_0^L \int_0^T B_c s_c u_c^2 \, dt \, dx, \tag{10a}$$

$$\int_0^L \int_0^T B_f C_d^f |u_f| u_f^2 \, dt \, dx = \int_0^L \int_0^T B_f s_f u_f^2 \, dt \, dx. \tag{10b}$$

In this study, the quadratic drag coefficients (C_d^c, C_d^f) and linearized friction coefficients (s_c, s_f) are assumed to be uniform along the estuary. Since u_c, u_f, s_c, and s_f are all unknown initially, they are iteratively determined based on the prescribed drag coefficients C_d^c and C_d^f, using an initial guess for s_c and s_f. Note that large values of C_d^c and C_d^f correspond to large s_c and s_f, that is, strong bottom friction.

2.2. Solution Techniques

The system of the water motion equations (Equations 3 and 7) is solved using a perturbation method. First, following Winant (2007), the non-dimensional form of these equations is derived using a scaling analysis, with variables in these water motion equations scaled with their typical scales in tidally dominated estuaries (Table 1). Next, the order of various terms in the non-dimensional equations is determined with respect to a small parameter ε [typically ~0.1 in many tidal estuaries (Hepkema et al., 2018)],

$$\varepsilon = \frac{a_m}{H_c^m}, \tag{11}$$

with H_c^m the channel depth at the mouth. Then, each non-dimensional physical variable ψ^* is expanded asymptotically in ε:

Table 1
Scales of Physical Variables

Variable	Typical scale	Symbol	Expression
t	Tidal frequency	σ	$\sigma^{-1}t^*$
$\left(\eta,\eta_c,\eta_f\right)$	Tidal amplitude at the mouth	a_m	$a_m\eta^*$
x	Estuary length	L	Lx^*
$\left(y,B_c,B_f\right)$	Channel width at the mouth	B_c^m	$B_c^m\left(y^*,B_c^*,B_f^*\right)$
$\left(z,H_c,H_f\right)$	Channel depth at the mouth	H_c^m	$H_c^m\left(z^*,H_c^*,H_f^*\right)$
$\left(u,u_c,u_f\right)$	Typical longitudinal velocity	$U = \varepsilon\sigma L$	$U\left(u^*,u_c^*,u_f^*\right)$
v	Typical lateral velocity	$V = \varepsilon\sigma B_c^m$	Vv^*
F_n	Typical lateral water transport	VH_c^m	$VH_c^m F_n^*$
M_n	Typical lateral momentum transport	UVH_c^m	$UVH_c^m M_n^*$
$\left(s_c,s_f\right)$	Typical slip parameter	$\left(\sigma H_c,\sigma\frac{H_f}{2}\right)$	$\left(\sigma H_c s_c^*,\sigma\frac{H_f}{2}s_f^*\right)$

$$\psi^* = \sum_{i=0}^{\infty}\varepsilon^i\psi_i^* = \psi_0^* + \varepsilon\psi_1^* + \varepsilon^2\psi_2^* + \ldots, \tag{12}$$

where the superscript asterisk (*) denotes dimensionless variables and the subscript numbers (0, 1, 2) represent the orders in the expansion. Finally, by collecting all terms at the same order of ε, a system of equations at each order is derived. In this study, we focus on the principal tidal constituent at the leading order that is, forced at the mouth, while neglecting residual circulation, overtides, and their influence on the leading-order tidal motion.

2.2.1. Scaling Analysis

In our scaling analysis, the time (t) is scaled with the tidal frequency (σ). The tidal elevations (η, η_c, η_f) are scaled with tidal amplitude at the mouth (a_m). The longitudinal (x), lateral (y, B_c, B_f), and vertical (z, H_c, H_f) coordinates/dimensions are assumed to scale with the estuary length (L), channel width at the mouth (B_c^m), and the channel depth at the mouth (H_c^m), respectively. The longitudinal (u, u_c, u_f) and lateral (v) tidal velocities are scaled with their typical scales in tidally dominated estuaries, $U = \varepsilon\sigma L$ and $V = \varepsilon\sigma B_c^m$, respectively. The lateral water (F_n) and momentum (M_n) exchanges are separately scaled with their typical scales VH_c^m and UVH_c^m. The typical scales of physical variables are summarized in Table 1.

Based on the typical scales of variables (Table 1), the dimensionless channel water motion equations (Equation 3) are derived:

$$\frac{\partial}{\partial x^*}\left[u_c^* B_c^*\left(H_c^* + \eta_c^*\varepsilon\right)\right] + B_c^*\frac{\partial\eta_c^*}{\partial t^*} + 2F_n^* = 0, \tag{13a}$$

$$\frac{\partial u_c^*}{\partial t^*} + \frac{U}{\sigma L}u_c^*\frac{\partial u_c^*}{\partial x^*} + \frac{V}{\sigma B_c^m}\frac{2\left(M_n^* - u_c^* F_n^*\right)}{B_c^*\left(H_c^* + \eta_c^*\varepsilon\right)} = -\frac{gH_c^m}{\sigma^2 L^2}\frac{\partial\eta_c^*}{\partial x^*} - \frac{H_c^* s_c^*}{H_c^* + \eta_c^*\varepsilon}u_c^*, \tag{13b}$$

The dimensionless intertidal water motion equations (Equation 7) read

$$\frac{\partial}{\partial x^*}\left[u_f^* B_f^*\frac{\left(H_f^* + \eta_f^*\varepsilon\right)^2}{4H_f^*}\right] + B_f^*\frac{H_f^* + \eta_f^*\varepsilon}{2H_f^*}\frac{\partial\eta_f^*}{\partial t^*} - F_n^* = 0, \tag{14a}$$

$$\frac{\partial u_f^*}{\partial t^*} + \frac{U}{\sigma L} u_f^* \frac{\partial u_f^*}{\partial x^*} - \frac{V}{\sigma B_c^m} \frac{4H_f^* \left(M_n^* - u_f^* F_n^*\right)}{B_f^* \left(H_f^* + \eta_f^* \varepsilon\right)^2} = -\frac{g H_c^m}{\sigma^2 L^2} \frac{\partial \eta_f^*}{\partial x^*} - \frac{H_f^* s_f^*}{H_f^* + \eta_f^* \varepsilon} u_f^*. \tag{14b}$$

The dimensionless lateral water exchange and momentum exchange between the intertidal and channel areas are

$$F_n^* = \frac{F_n}{V H_c^m} = \int_{-h^*}^{\eta^* \varepsilon} \left(-\frac{1}{2} \frac{dB_c^*}{dx^*} u^*, \pm v^*\right) dz^* \bigg|_{y^* = \pm \frac{B_c^*}{2}}, \tag{15a}$$

$$M_n^* = \frac{M_n}{U V H_c^m} = \int_{-h^*}^{\eta^* \varepsilon} u^* \left(-\frac{1}{2} \frac{dB_c^*}{dx^*} u^*,\ \pm v^*\right) dz^* \bigg|_{y^* = \pm \frac{B_c^*}{2}}. \tag{15b}$$

The dimensionless seaward and landward boundary conditions (Equations 6 and 8) read

$$\eta_c^* = \eta_f^* = \cos t^*, \text{at } x^* = 0, \tag{16a}$$

$$u_c^* B_c^* \left(H_c^* + \eta_c^* \varepsilon\right) + u_f^* B_f^* \frac{\left(H_f^* + \eta_f^* \varepsilon\right)^2}{2H_f^*} = -\frac{Q}{U B_c^m H_c^m}, \text{at } x^* = 1. \tag{16b}$$

For tidally dominated estuaries, the river discharge term $Q/UB_c^m H_c^m$ is of order ε (Chernetsky et al., 2010; Kumar et al., 2016). Following Winant (2007), the barotropic pressure gradient parameter $gH_c^m/\sigma^2 L^2$ is taken as $O(1)$, while the advection parameters $U/\sigma L$ and $V/\sigma B_c^m$ are of order $O(\varepsilon)$ in tidally dominated estuaries. The orders of magnitude of all dimensionless parameters in the scaling analysis are summarized in Table S2 of the Supporting Information S1.

Therefore, in tidally dominated estuaries considered in this study, the leading-order water motion is determined by the tidal constituent prescribed at the seaward boundary, while the effects of advection and river discharge appear at higher orders. Besides, the water and momentum exchanges (F_n and M_n, driving the lateral exchange term in the momentum equations) do not arrive at the leading-order momentum equations because they are higher-order terms. This means that the coupling between the longitudinal flow in the channel and over the intertidal area is directly driven by the water exchange F_n in the continuity equations (i.e., ensuring the water mass balance, see Equation 22), with the momentum equations resolved independently within each region (see Equation 24).

By substituting the expansion (Equation 12) into the above water motion equations (Equations 13–16) and collecting all terms at $O(1)$, the governing equations for the leading-order tidal water motion in the channel are derived (see Text S3 in Supporting Information S1):

$$\frac{\partial}{\partial x}\left(u_{c_0} B_c H_c\right) + B_c \frac{\partial \eta_{c_0}}{\partial t} + 2F_{n_0} = 0, \tag{17a}$$

$$\frac{\partial u_{c_0}}{\partial t} = -g \frac{\partial \eta_{c_0}}{\partial x} - \frac{s_c}{H_c} u_{c_0}. \tag{17b}$$

The leading-order tidal water motion over the intertidal region is governed by

$$\frac{\partial}{\partial x}\left(u_{f_0} B_f \frac{H_f}{4}\right) + \frac{B_f}{2} \frac{\partial \eta_{f_0}}{\partial t} - F_{n_0} = 0, \tag{18a}$$

$$\frac{\partial u_{f_0}}{\partial t} = -g \frac{\partial \eta_{f_0}}{\partial x} - \frac{2s_f}{H_f} u_{f_0}, \tag{18b}$$

with the leading-order water exchange

$$F_{n_0} = \int_{-h}^{0} (u_0, v_0) \cdot \boldsymbol{n}_{\mathrm{h}} dz \Big|_{y=\pm\frac{B_c}{2}}. \tag{19}$$

The leading-order seaward and landward boundary conditions read

$$\eta_{c_0} = \eta_{f_0} = a_m \cos(\sigma t), \text{at } x = 0, \tag{20a}$$

$$u_{c_0} B_c H_c + u_{f_0} B_f \frac{H_f}{2} = 0, \text{at } x = L. \tag{20b}$$

The leading-order Lorentz linearization of the bottom friction in the channel and intertidal area are respectively described by

$$\int_0^L \int_0^T B_c C_d^c |u_{c_0}| (u_{c_0})^2 dt\, dx = \int_0^L \int_0^T B_c s_c (u_{c_0})^2 dt\, dx, \tag{21a}$$

$$\int_0^L \int_0^T B_f C_d^f |u_{f_0}| (u_{f_0})^2 dt\, dx = \int_0^L \int_0^T B_f s_f (u_{f_0})^2 dt\, dx. \tag{21b}$$

Combining the continuity equations for the channel (Equation 17a) and intertidal area (Equation 18a), it yields

$$\frac{\partial}{\partial x}(u_{c_0} B_c H_c) + B_c \frac{\partial \eta_{c_0}}{\partial t} + \overbrace{\frac{\partial}{\partial x}\left(u_{f_0} B_f \frac{H_f}{2}\right)}^{F_{n_0}^{\mathrm{ILC}}} + \overbrace{B_f \frac{\partial \eta_{f_0}}{\partial t}}^{F_{n_0}^{\mathrm{IWS}}} = 0, \tag{22}$$

with $\eta_{c_0} = \eta_{f_0}$. Equation 22 shows that the leading-order tidal propagation in the channel is affected by the water exchange between the channel and intertidal areas: $F_{n_0} = F_{n_0}^{\mathrm{ILC}} + F_{n_0}^{\mathrm{IWS}}$. The first contribution, $F_{n_0}^{\mathrm{ILC}}$ [ignored in previous analytical models (e.g., Jay, 1991; Friedrichs & Madsen, 1992)], arises from the divergence of longitudinal water flux in the intertidal area due to non-zero longitudinal currents over intertidal areas (referred to as ILC hereinafter). The second contribution, $F_{n_0}^{\mathrm{IWS}}$, arises from the temporal variations of water storage over intertidal areas (referred to as IWS hereinafter).

To solve Equation 22 analytically, the leading-order velocities and water levels are expressed in a complex form:

$$\left(u_{c_0}, \eta_{c_0}, u_{f_0}, \eta_{f_0}\right) = \Re\left\{\left(\hat{u}_{c_0}, \hat{\eta}_{c_0}, \hat{u}_{f_0}, \hat{\eta}_{f_0}\right) e^{i\sigma t}\right\}, \tag{23}$$

where the hat $(\hat{\cdot})$ indicates the complex amplitude and $\Re\{\cdot\}$ denotes the real part of a complex variable. By substituting Equation 23 into the momentum Equations 17b and 18b, the complex amplitude of tidal velocities in the channel and intertidal areas are separately written as functions of longitudinal sea surface gradients:

$$\hat{u}_{c_0} = \beta_c \frac{d\hat{\eta}_{c_0}}{dx}, \hat{u}_{f_0} = \beta_f \frac{d\hat{\eta}_{f_0}}{dx}, \tag{24a}$$

with the proportionality coefficients

$$\beta_c = \frac{gi}{\sigma} \frac{1}{1 - is_c^*}, \beta_f = \frac{gi}{\sigma} \frac{1}{1 - is_f^*}. \tag{24b}$$

Substituting Equation 23 into Equation 21 also yields the complex form of the Lorentz linearization condition:

$$\int_0^L \frac{8}{3} B_c C_d^c |\hat{u}_{c_0}|^3 dx = \int_0^L \pi B_c s_c |\hat{u}_{c_0}|^2 dx, \tag{25a}$$

$$\int_0^L \frac{8}{3} B_f C_d^f |\hat{u}_{f_0}|^3 dx = \int_0^L \pi B_f s_f |\hat{u}_{f_0}|^2 dx. \tag{25b}$$

In estuaries with intertidal zones characterized by extremely high friction (i.e., $C_d^f \to \infty$; $s_f^* \to \infty$), the parameter β_f approaches zero, causing the longitudinal currents over intertidal areas to vanish. This yields the same solution as previous analytical studies where the current velocity over intertidal areas u_{f_0} and the ILC-induced water exchange $F_{n_0}^{\mathrm{ILC}}$ are neglected (e.g., Jay, 1991).

By substituting Equations 23 and 24 into Equation 22, the coupled equation for the complex tidal amplitudes in the channel and intertidal areas is derived:

$$\frac{d}{dx}\left(\beta_c B_c H_c \frac{d\hat{\eta}_{c_0}}{dx}\right) + i\sigma B_c \hat{\eta}_{c_0} + \frac{d}{dx}\left(\beta_f B_f \frac{H_f}{2} \frac{d\hat{\eta}_{f_0}}{dx}\right) + i\sigma B_f \hat{\eta}_{f_0} = 0. \tag{26}$$

Recalling $\hat{\eta}_{f_0} = \hat{\eta}_{c_0}$, Equation 26 becomes a second-order ordinary differential equation

$$T_1(x)\frac{d^2\hat{\eta}_{c_0}}{dx^2} + T_2(x)\frac{d\hat{\eta}_{c_0}}{dx} + T_3(x)\hat{\eta}_{c_0} = 0, \tag{27}$$

with

$$T_1(x) = \beta_c B_c H_c + \beta_f B_f \frac{H_f}{2}, \tag{28a}$$

$$T_2(x) = \frac{d}{dx}(\beta_c B_c H_c) + \frac{d}{dx}\left(\beta_f B_f \frac{H_f}{2}\right), \tag{28b}$$

$$T_3(x) = i\sigma B_c + i\sigma B_f. \tag{28c}$$

By substituting Equation 23 into Equation 20, the seaward and landward boundary conditions are derived

$$\hat{\eta}_{c_0} = a_m, \text{at } x = 0, \tag{29a}$$

$$\frac{d\hat{\eta}_{c_0}}{dx} = 0, \text{at } x = L. \tag{29b}$$

For estuaries with spatially varying geometry $[B_c(x), B_f(x)]$ and bathymetry $[H_c(x), H_f(x)]$, the coupled tidal wave equation (Equation 27) can be solved semi-analytically, using a finite difference method.

2.2.2. Analytical Solution

To derive an analytical solution for Equation 27, we consider idealized estuaries with a longitudinally uniform bathymetry (i.e., constant H_c, H_f) and an exponentially converging width in the channel and over the intertidal area:

$$\frac{B_c}{B_c^m} = \frac{B_f}{B_f^m} = e^{-\frac{x}{L_e}}. \tag{30}$$

Here B_c^m and B_f^m are the width of the channel and intertidal areas at the mouth, respectively. By assuming the convergence length (L_e) of the channel and the intertidal zones to be identical, the ratio of the intertidal width to the channel width, denoted by r_B, remains constant along the estuary,

$$r_B = \frac{B_f}{B_c} = \frac{B_f^m}{B_c^m}. \tag{31}$$

For these idealized estuaries, the complex amplitude of the leading-order tidal elevation can be solved analytically:

$$\begin{aligned}\hat{\eta}_{c_0} &= a_m e^{\frac{x}{2L_e}} \frac{\left[1+(2L_e ik)^{-1}\right] e^{ik(L-x)} + \left[1-(2L_e ik)^{-1}\right] e^{-ik(L-x)}}{\left[1+(2L_e ik)^{-1}\right] e^{ikL} + \left[1-(2L_e ik)^{-1}\right] e^{-ikL}} \\ &= a_m e^{\frac{x}{2L_e}} \frac{\cosh[ik(L-x)] + (2L_e ik)^{-1}\sinh[ik(L-x)]}{\cosh(ikL) + (2L_e ik)^{-1}\sinh(ikL)}.\end{aligned} \tag{32}$$

Here, $k = \sqrt{T_3/T_1 - (T_2/2T_1)^2} = k_r + ik_i$ is the complex tidal wavenumber, with k_r and k_i as its real and imaginary parts, respectively. Here, $k_r \geq 0$ is the conventional tidal wavenumber, and $k_i \leq 0$ is the damping modulus, which measures the exponential decay rate of the incident ($e^{ik(L-x)}$) and reflected ($e^{-ik(L-x)}$) waves (Talke & Jay, 2020; J. J. Dronkers, 1964; Hunt, 1964; Kästner et al., 2019). Therefore, an increase in k_r and a more negative k_i correspond respectively to a reduction in tidal celerity (or wavelength) and an increase in the damping rate of incident and reflected waves. This solution shares the same form as that derived by Jay (1991) for exponentially convergent estuaries, where tidal propagation is determined by two dimensionless parameters kL and L_e/L.

In the presence of intertidal zones, that is, considering both the IWS and ILC effects on the channel-intertidal water exchange, the complex tidal wavenumber (k) becomes

$$k^{\mathrm{F}} = \frac{2\pi}{\lambda_c}\sqrt{\frac{1+r_B}{1+r_F}\left(\underbrace{1}_{\text{local inertia}} - \underbrace{is_c^*}_{\text{dissipation}}\right) - \underbrace{(\Delta_e)^2}_{\text{convergence}}}, \tag{33}$$

with

$$r_F = r_B r_H \frac{1-is_c^*}{1-is_f^*}, r_H = \frac{H_f}{2H_c}, \lambda_c = T\sqrt{gH_c}, \text{and } \Delta_e = \frac{1}{2\pi}\frac{\lambda_c}{2L_e}. \tag{34}$$

Here, r_F is the ratio of the complex amplitude of the longitudinal water flux integrated over the intertidal area to that integrated over the channel, r_H is the ratio of the mean intertidal water depth to the channel water depth, λ_c represents the frictionless tidal wavelength in straight channels without any intertidal areas, and Δ_e is the dimensionless convergence parameter. Equation 33 shows that the complex tidal wavenumber is influenced by r_B, r_F, L_e, s_c^*, and λ_c through their effects on the local inertia ($\partial_t u_{c_0}$), bottom friction/dissipation (s_c^*), and width convergence (Δ_e), as noted by Jay (1991) and Talke and Jay (2020).

In the absence of any intertidal zones ($r_B = 0$ and $r_F = 0$), the channel-intertidal water exchange is zero, and k becomes

$$k^{\mathrm{N}} = \frac{2\pi}{\lambda_c}\sqrt{\underbrace{1}_{\text{local inertia}} - \underbrace{is_c^*}_{\text{dissipation}} - \underbrace{(\Delta_e)^2}_{\text{convergence}}}. \tag{35}$$

This solution is the same as that derived by Jay (1991) and Talke and Jay (2020).

When considering only the IWS effect on the channel-intertidal water exchange and neglecting the ILC effect ($r_F = 0$), k becomes

$$k^{\mathrm{IWS}} = \frac{2\pi}{\lambda_c}\sqrt{(1+r_B)\left(\underbrace{1}_{\text{local inertia}} - \underbrace{is_c^*}_{\text{dissipation}}\right) - \underbrace{(\Delta_e)^2}_{\text{convergence}}}. \tag{36}$$

This formulation is the same as that derived by Jay (1991) and Winterwerp and Wang (2013), which considers the effects of intertidal areas on the water storage capacity only.

As shown in Equation 34, the water flux ratio r_F is a function of the width ratio r_B, the depth ratio r_H, and the velocity ratio $\left(1 - is_c^*\right)/\left(1 - is_f^*\right)$ between the intertidal and channel regions (as defined in Equations 24a and 24b). In realistic estuaries, since the depth and velocity in the intertidal area are less than those in the channel, the magnitude of r_F is less than r_B: $|r_F/r_B| < 1$. If the channel and intertidal regions are either frictionless ($s_c^* \ll 1$; $s_f^* \ll 1$) or strongly frictional ($s_c^* \gg 1$; $s_f^* \gg 1$), the flux ratio r_F approaches a real number,

$$r_F = \begin{cases} r_B r_H, \text{for } s_c^* \ll 1 \text{ and } s_f^* \ll 1 \\ r_B r_H \dfrac{s_c^*}{s_f^*}, \text{for } s_c^* \gg 1 \text{ and } s_f^* \gg 1 \end{cases}. \tag{37}$$

Equation 33 shows that the IWS effect increases the local inertia and dissipation terms by a factor of $1 + r_B$, whereas the ILC effect decreases both terms by a factor of $1/(1 + r_F)$. Nevertheless, intertidal areas do not alter the convergence term in the complex wavenumber. Equation 32 also shows that resonance (Miles, 1971) occurs as its denominator approaches zero: $\cosh(ikL) + (2L_e ik)^{-1}\sinh(ikL) = 0$, which yields

$$\frac{\tan(k_r L)}{k_r L} + \frac{2L_e}{L} = 0, \tag{38}$$

and $k_i L = 0$. Equation 38 reveals a strong dependence of tidal wave resonance on L_e/L. Since the complex tidal wavenumber is influenced by the effects of intertidal areas (Equation 33), changes in the estuarine intertidal zone can alter the resonant characteristics of tidal waves in semi-enclosed estuaries. We will show in Section 3 that the inclusion of intertidal zones in an estuary can move the system either closer to or farther from the resonance condition, as reported by Rainey (2009).

3. Results

3.1. Tidal Wavenumber and Resonance

In convergent estuaries with a reflective landward boundary, tides can be either amplified or damped along the estuary due to interference between incident and reflected waves and bottom friction (Talke & Jay, 2020). In these estuaries, the energy of the incident wave is funneled landward into increasingly smaller cross-sections where it is reflected and travels seaward. Meanwhile, the reflected wave tends to dampen quickly as it moves seaward as a result of both width divergence and bottom friction (Green, 1837). Consequently, in these systems, the interference between the incident and reflected waves is typically most prominent at the head. Also, tides are more variable upstream due to the cumulative effects of tidal changes further seaward (Talke & Jay, 2020). Therefore, the largest tidal responses to changes in estuary parameters (e.g., depth, width, friction) are usually found near the head of reflective converging systems (Chernetsky et al., 2010; Ensing et al., 2015; Ralston et al., 2019; Winterwerp et al., 2013), although exceptions may occur in some estuaries (e.g., the middle reach of the Scheldt estuary, Winterwerp et al., 2013). For simplicity, our analysis focuses on the effects of intertidal areas at the head. Following Alebregtse et al. (2013) and Roos and Schuttelaars (2015), we define the amplification factor (A_*),

$$A_* = \frac{\hat{\eta}_{c0}\big|_{x=L}}{a_m} = e^{\frac{L}{2L_e}} \frac{1}{\cosh(ikL) + (2L_e ik)^{-1}\sinh(ikL)}, \tag{39}$$

to measure the tidal amplification/damping at the head, where its magnitude and argument represent the amplitude ratio and phase difference between tides at the head and those at the mouth. Equation 39 shows strong dependence of tidal amplification/damping on kL and L_e/L, and the resonance (Equation 38) leads to $A_* \to \infty$. By comparing A_* calculated with different tidal wavenumbers (Equations 33, 35, and 36), the effects of intertidal areas resulting from the IWS and ILC effects can be separated.

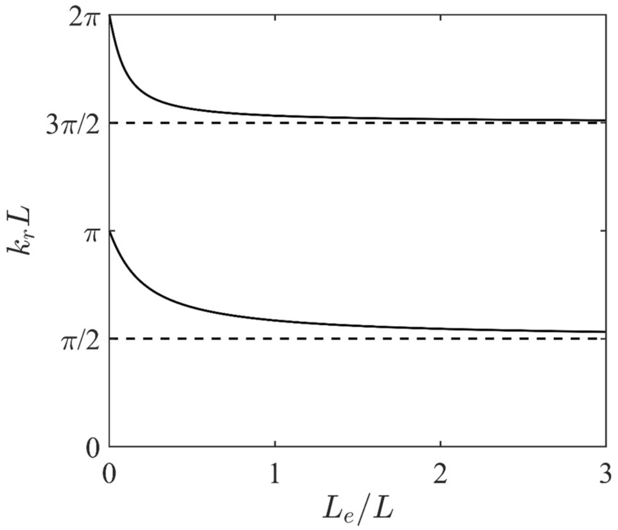

Figure 2. Dependence of k_rL on L_e/L under the resonance condition where $k_iL = 0$ and $|A_*| \to \infty$ (Equation 38). The dashed lines indicate values of the resonant k_rL when $L_e/L \to \infty$, that is, straight estuaries.

The effect of intertidal areas on the complex wavenumber k has strong implications for tidal propagation in estuaries by modifying the resonance characteristics of the tidal wave. The value of k_rL at which resonance occurs (hereafter referred to as the resonant k_rL) decreases as L_e/L increases (Figure 2). The resonant k_rL approaches $\pi/2$ or $3\pi/2$ as L_e/L becomes infinite (i.e., straight estuaries), corresponding to the quarter or three-quarter wave resonant length (Talke & Jay, 2020). As real estuaries are rarely influenced by the second resonant mode (Talke & Jay, 2020), the discussion hereafter focuses on the impact of intertidal areas on the first resonant mode ($\pi/2 < k_rL < \pi$).

Both the amplitude and phase of the amplification factor A_* are strongly sensitive to the nondimensional complex tidal wavenumber k_rL and k_iL together with L_e/L (Figure 3). For k_rL less than its resonant value (with $|A_*| \to \infty$), any increase in k_rL results in enhanced tidal amplification (i.e., increased $|A_*|$), and vice versa (Figures 3a and 3c). For k_rL larger than its resonant value, however, increases in k_rL lead to more tidal damping

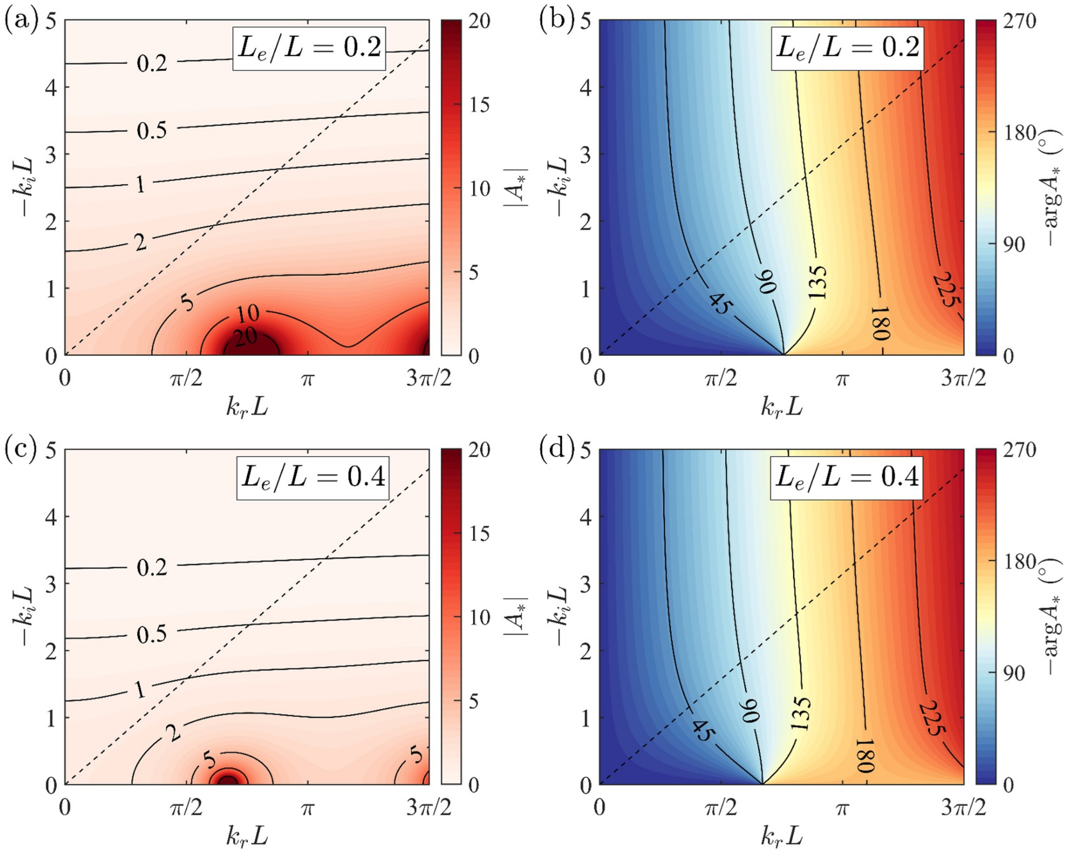

Figure 3. (a) Amplitude and (b) phase of A_* (obtained from Equation 39) as a function of k_rL and $-k_iL$ for $L_e/L = 0.2$ (typical of the Ribble estuary, J. Dronkers, 2016). (c), (d) Same as (a), (b) but for $L_e/L = 0.4$ (typical of Darwin Harbour, L. Li et al., 2012). The dashed lines represent the condition $k_rL = -k_iL$.

Table 2
ILC Effects on Tidal Wavenumber and Tidal Propagation in Different Systems

Type number	Type of systems	Dominant processes	Parameter space of kL	ILC effect on kL	ILC effect on tidal propagation
1	Weakly dissipative, weakly convergent	Local inertia	$-k_iL \rightarrow 0$	Decrease k_rL	Damping or amplification
2	Moderately dissipative, weakly convergent	Local inertia, bottom friction	$0 < -k_iL < k_rL$	Between Types 1 and 3	
3	Strongly dissipative, weakly/moderately convergent	Bottom friction	$k_rL \rightarrow -k_iL$	Decrease k_rL and $-k_iL$	Amplification
4	Strongly dissipative, strongly convergent	Bottom friction, convergence	$-k_iL > k_rL > 0$	Between Types 3 and 5	
5	Weakly/moderately dissipative, strongly convergent	Convergence	$k_rL \rightarrow 0$	Minor	Minor
6	Weakly dissipative, moderately convergent	Local inertia, convergence	$k_rL \rightarrow 0$, or $-k_iL \rightarrow 0$	Between Types 1 and 5	
7	Moderately dissipative, moderately convergent	All	$k_rL > 0$ and $-k_iL > 0$	Highly variable, depending on the processes involved	

(i.e., decreased $|A_*|$). Since k_i is the damping modulus, increases in $-k_iL$ cause more tidal damping. Increases in k_rL also result in more delayed tidal propagation, whereas increases in $-k_iL$ can lead to slightly more delayed or advanced tidal propagation depending on k_rL (Figures 3b and 3d). Increasing L_e/L from 0.2 to 0.4 significantly reduces the magnitude of A_* (comparing Figures 3a and 3c). This implies that tides are more likely to amplify along estuaries ($|A_*| > 1$) with stronger width convergence (i.e., a smaller L_e/L). The phase of A_* is slightly modified by increasing L_e/L due to a decrease in the resonant k_rL (Figures 3b and 3d).

As shown by Equations 33 and 34, the nondimensional wavenumber (k_rL, $-k_iL$) is affected by intertidal zones through modulating the width and water flux ratios between the intertidal and channel regions (r_B and r_F). Also, the effects of intertidal areas on tidal amplification/damping are dependent on the distance between the wavenumber (k_rL, $-k_iL$) and its resonant value (determined by Equation 38), which can vary across estuaries with different characteristics. Inspired by Jay (1991) and Lanzoni and Seminara (1998), we consider seven distinct systems (see Table 2) according to the relative importance of local inertia, estuary width convergence, and bottom friction, to systematically understand the effects of intertidal areas on estuarine tidal propagation under various conditions.

3.1.1. Weakly Dissipative and Weakly Convergent Estuaries

In weakly dissipative and weakly convergent estuaries [$(\Delta_e)^2 \ll 1$; $s_c^* \ll 1$; $s_f^* \ll 1$, where the unity represents the typical order of local inertia, see Equation 33], tidal propagation is dominated by local inertia. The nondimensional complex tidal wavenumber reduces to

$$kL = 2\pi \frac{L}{\lambda_c} \sqrt{\frac{1 + r_B}{1 + r_F}}, \tag{40}$$

with $r_F = r_B r_H$ as a real number (Equation 37). Under this condition, kL becomes a real number, that is, $-k_iL \rightarrow 0$. Intertidal areas increase k_rL by a factor of $\sqrt{1 + r_B}$ through IWS but decrease it by a factor of $1/\sqrt{1 + r_F}$ through ILC. Since r_B is typically larger than r_F in estuaries (as discussed in Section 2.2.2), intertidal areas lead to an overall increase in k_rL in these estuaries. Hence, for k_rL less than its resonant value, the existence of intertidal areas brings the system closer to resonance by increasing k_rL, causing tidal amplification. For k_rL above the resonant value, the increase in k_rL due to intertidal areas causes tidal damping (see Figures 3a and 3c). The ILC effect, however, contributes oppositely to the total effect of intertidal areas by decreasing k_rL, causing tidal damping for small k_rL values and tidal amplification for large k_rL values.

Due to the linear relationship between kL and L/λ_c (Equation 40), the nondimensional tidal wavenumber k_rL increases with increasing estuary length L and decreasing tidal wavelength λ_c (e.g., with smaller channel depth H_c or larger tidal frequency σ), despite the water flux ratio r_F increasing with decreasing H_c. Since r_F is dependent on

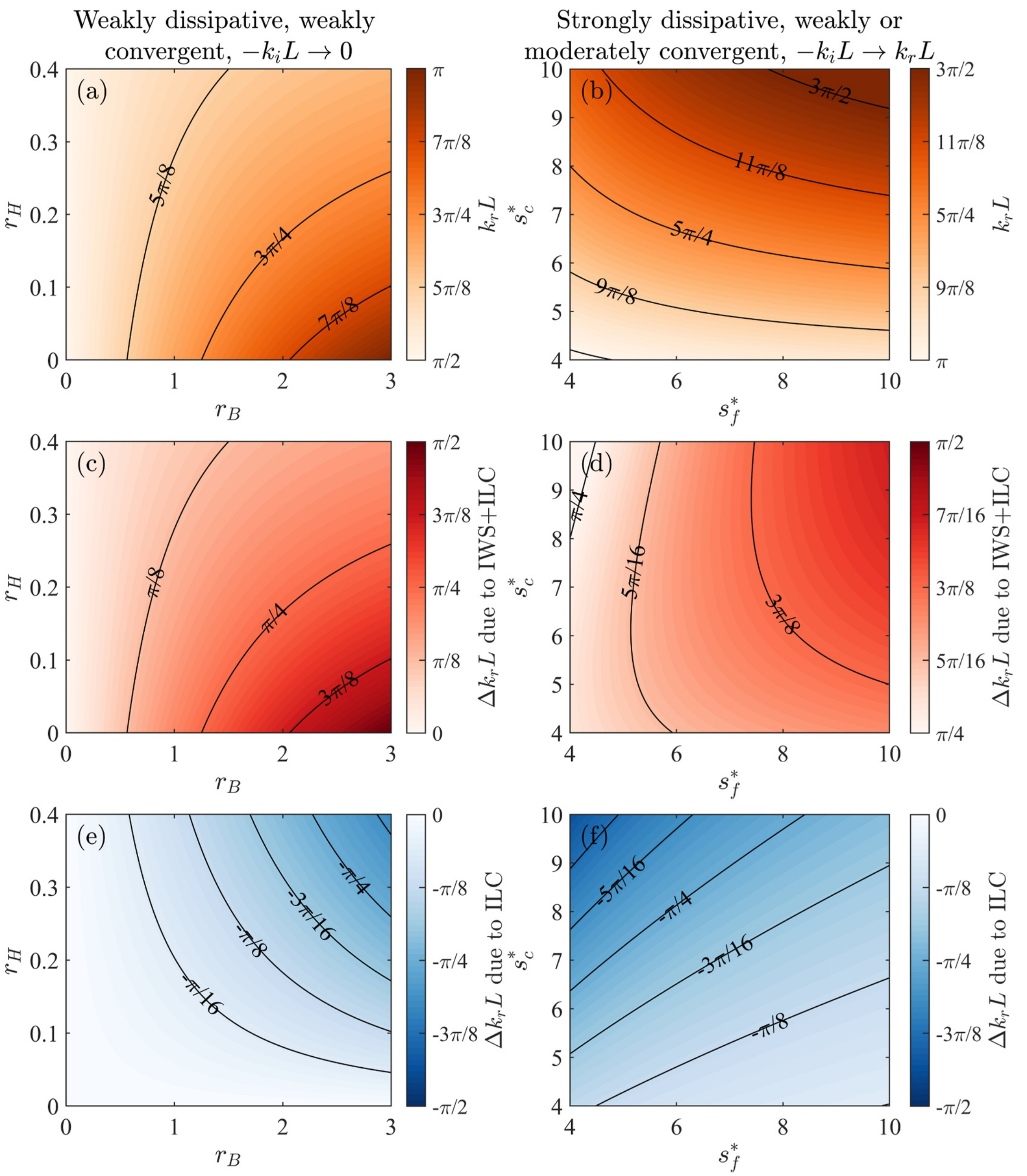

Figure 4. Real part of the nondimensional wavenumber (k_rL) as a function of (a) the width ratio and depth ratio between the intertidal and channel areas (r_B and r_H) in weakly dissipative and weakly convergent systems, and (b) the dimensionless bottom friction parameters of the intertidal and channel regions (s_f^* and s_c^*) in strongly dissipative and weakly or moderately convergent systems for $r_B = 1.5$ and $r_H = 0.2$ (representative of the Ribble estuary, van der Wal et al., 2002). (c), (d) Same as (a), (b) but for the changes in k_rL due to the overall effects of intertidal areas including both IWS and ILC: $\Delta k_rL = k_r^{\mathrm{F}}L - k_r^{\mathrm{N}}L$. (e), (f) Same as (a), (b) but for the changes in k_rL due to ILC only, that is, $\Delta k_rL = k_r^{\mathrm{F}}L - k_r^{\mathrm{IWS}}L$. Here, the values of k_rL and Δk_rL, which are proportional to L/λ_c, are calculated with $L/\lambda_c = 1/4$ as an example.

the width ratio r_B and the depth ratio r_H between the intertidal and channel regions, k_rL is also a function of r_B and r_H. As shown in Figure 4a, k_rL significantly increases with decreasing the depth ratio r_H and/or increasing the width ratio r_B. The increases in k_rL (positive Δk_rL) due to the total effects of intertidal areas are more pronounced for smaller r_H and larger r_B (Figure 4c), where k_rL is larger (Figure 4a). However, the decreases in k_rL (negative Δk_rL) due to the ILC effect are more considerable for larger r_H and larger r_B, where the water flux ratio r_F is larger (Equation 34) and the ILC effect on k_rL exceeds the overall effects of intertidal areas (Figure 4e).

This also implies that estuaries with shorter lengths, deeper channels, deeper and narrower intertidal zones, forced by lower-frequency tides tend to have smaller tidal wavenumbers, where the intertidal area tends to amplify tides and its ILC contribution causes tidal damping, and vice versa. The variable effects of intertidal areas on tidal amplification/damping in weakly dissipative and weakly convergent estuaries are consistent with the different responses of estuaries to changing conditions discussed in Talke and Jay (2020). They found that, in straight frictionless estuaries ($L_e/L \to \infty$), the quarter-wave resonance occurs at $k_rL = \pi/2$ (as shown in Figure 2). Consequently, a reduction in channel depth leads to tidal amplification for estuaries with $L/\lambda_c < 1/4$, and tidal damping for estuaries with $L/\lambda_c > 1/4$. As the presence of shallow intertidal regions effectively reduces the mean water depth over the total cross-section (as discussed in Section 4.1), the effects of intertidal areas on tidal propagation can shift from tidal amplification to damping when k_rL exceeds $\pi/2$.

3.1.2. Strongly Dissipative and Weakly or Moderately Convergent Estuaries

In strongly dissipative and weakly or moderately convergent estuaries [$s_c^* \gg 1$; $s_f^* \gg 1$; $(\Delta_e)^2 \le O(1)$], tidal propagation is dominated by bottom friction. The nondimensional complex tidal wavenumber reduces to

$$kL = 2\pi \frac{L}{\lambda_c} \frac{1-i}{\sqrt{2}} \sqrt{\frac{1+r_B}{1+r_F} s_c^*}, \tag{41}$$

with $r_F = r_B r_H s_c^* / s_f^*$ as a real number (Equation 37). Under this condition, the real part of kL approaches the magnitude of its imaginary part: $k_rL \to -k_iL$, as observed by Jay (1991). This condition can also occur when the local inertial and estuary convergence effects nearly cancel each other (i.e., critical convergence, Jay, 1991). In these estuaries, the IWS effect tends to increase k_rL and $-k_iL$ by a factor of $\sqrt{1 + r_B}$, while the ILC effect tends to decrease both parameters by a factor of $1/\sqrt{1 + r_F}$. Consequently, the total effect of intertidal areas causes an increase in both k_rL and $-k_iL$ (due to $r_F/r_B < 1$). Regardless of the values of L_e/L, the magnitude of A_* can be proved to consistently decrease as kL increases along $k_rL = -k_iL$ (e.g., dashed lines in Figures 3a and 3c). This means that in these estuaries, the increases in tidal wavenumber due to intertidal areas consistently cause tidal damping, while the ILC effect causes tidal amplification by decreasing the wavenumber.

In addition to the aforementioned dependence of kL on L, H_c, σ, H_f, and r_B, Equation 41 also demonstrates a dependence of kL on the intertidal bottom friction s_f^* (through r_F) and channel bottom friction s_c^*. Figure 4b shows that both the real and imaginary parts of kL considerably increase with increasing s_c^* [consistent with Jay (1991)] and s_f^*, and kL is more sensitive to s_c^* than s_f^*. Besides, the increases in k_rL (Δk_rL) due to the overall effects of intertidal areas are more pronounced for larger s_c^* and s_f^* (Figure 4d), where k_rL is larger (Figure 4b), despite a slight reduction in Δk_rL with increasing s_c^* under small s_f^* conditions. Also, Δk_rL associated with the ILC effect is more significant for larger s_c^* and smaller s_f^*, where the water flux ratio r_F is higher (Equation 34) and the ILC contribution to Δk_rL are comparable to those induced by the overall effects of intertidal areas (Figure 4f).

3.1.3. Weakly or Moderately Dissipative and Strongly Convergent Estuaries

In weakly or moderately dissipative and strongly convergent estuaries [$s_c^* \le O(1)$; $s_f^* \le O(1)$; $(\Delta_e)^2 \gg 1$], tidal propagation is dominated by estuary width convergence. The nondimensional complex tidal wavenumber reduces to an imaginary number:

$$kL = -\frac{L}{2L_e} i, \tag{42}$$

with $k_rL \to 0$, as found by Jay (1991). Equation 42 shows that intertidal areas have minor effects on k in these estuaries, with negligible effects of intertidal areas on tidal propagation.

Due to the dependence of kL on L/L_e, the value of $-k_iL$ increases with decreasing estuary convergence length (increasing width convergence) relative to the estuary length [see also in Jay (1991)]. In addition to strong width convergence, low-frequency tidal forcings ($\sigma \to 0$) can also lead to convergence-dominated conditions, with

$\Delta_e \rightarrow \infty$ and $k_r L \rightarrow 0$ (see Equations 33 and 34). This implies that lower-frequency tidal waves (e.g., residual components) are hardly affected by the intertidal processes.

3.1.4. Weakly Dissipative and Moderately Convergent Estuaries

Based on the aforementioned three specific estuary types, we can further identify four intermediate systems. In weakly dissipative and moderately convergent estuaries [$s_c^* \ll 1$; $s_f^* \ll 1$; $(\Delta_e)^2 = O(1)$], tidal propagation is controlled by local inertia and estuary width convergence. The nondimensional complex tidal wavenumber becomes

$$kL = 2\pi \frac{L}{\lambda_c} \sqrt{\frac{1 + r_B}{1 + r_F} - (\Delta_e)^2}. \tag{43}$$

Here, $r_F = r_B r_H$ is a real number (Equation 37). Hence, $k_r L \rightarrow 0$ if width convergence effects are stronger than local inertia; and $-k_i L \rightarrow 0$ when local inertia effects are stronger. In these systems, the effects of intertidal areas on tides are between those in weakly dissipative, weakly convergent estuaries (Section 3.1.1) and those in weakly/moderately dissipative, strongly convergent estuaries (Section 3.1.3). In these estuaries, intertidal zones cause tidal amplification for small $k_r L$ values and tidal damping for large $k_r L$ values, and these effects weaken as width convergence increases. However, the ILC effect contributes oppositely to these tidal changes.

3.1.5. Strongly Dissipative and Strongly Convergent Estuaries

In strongly dissipative and strongly convergent estuaries [i.e., $s_c^* \gg 1$; $s_f^* \gg 1$; $(\Delta_e)^2 \gg 1$], tidal propagation is controlled by width convergence and bottom friction. The nondimensional complex tidal wavenumber reads

$$kL = 2\pi \frac{L}{\lambda_c} \sqrt{-\frac{1 + r_B}{1 + r_F} i s_c^* - (\Delta_e)^2}, \tag{44}$$

with $k_r L > 0$ and $-k_i L > k_r L$. Here, $r_F = r_B r_H s_c^* / s_f^*$ is a real number (Equation 37). Under this condition, the effects of intertidal areas on tides are between those in strongly dissipative, weakly/moderately convergent estuaries (Section 3.1.2) and those in weakly/moderately dissipative, strongly convergent estuaries (Section 3.1.3). In these estuaries, intertidal zones also consistently cause tidal damping while ILC leads to tidal amplification, and these effects become weaker for stronger width convergence.

3.1.6. Moderately Dissipative and Weakly Convergent Estuaries

In moderately dissipative and weakly convergent estuaries [$s_c^* = O(1)$; $s_f^* = O(1)$; $(\Delta_e)^2 \ll 1$], tidal propagation is controlled by local inertia and bottom friction. The nondimensional complex wavenumber reduces to

$$kL = 2\pi \frac{L}{\lambda_c} \sqrt{\frac{1 + r_B}{1 + r_F} (1 - i s_c^*)}, \tag{45}$$

with $k_r L > 0$ and $0 < -k_i L < k_r L$ [consistent with the weak convergence scenario discussed in Jay (1991)]. Here, r_F is a complex number (Equation 34). Under this condition, the effects of intertidal areas on tides are between those in weakly dissipative, weakly convergent estuaries (Section 3.1.1) and those in strongly dissipative, weakly/moderately convergent estuaries (Section 3.1.2). In these estuaries, when $-k_i L$ is small, the intertidal zones lead to tidal amplification for small $k_r L$ values and tidal damping for large $k_r L$ values, but when $-k_i L$ is large, intertidal areas tend to consistently dampen tides, and ILC contributes oppositely to these tidal changes.

3.1.7. Moderately Dissipative and Moderately Convergent Estuaries

In moderately dissipative and moderately convergent estuaries [$s_c^* = O(1)$; $s_f^* = O(1)$; $(\Delta_e)^2 = O(1)$], tidal propagation is controlled by local inertia, estuary convergence, and bottom friction altogether (i.e., $k_r L > 0$ and $-k_i L > 0$), as shown in Equation 33.

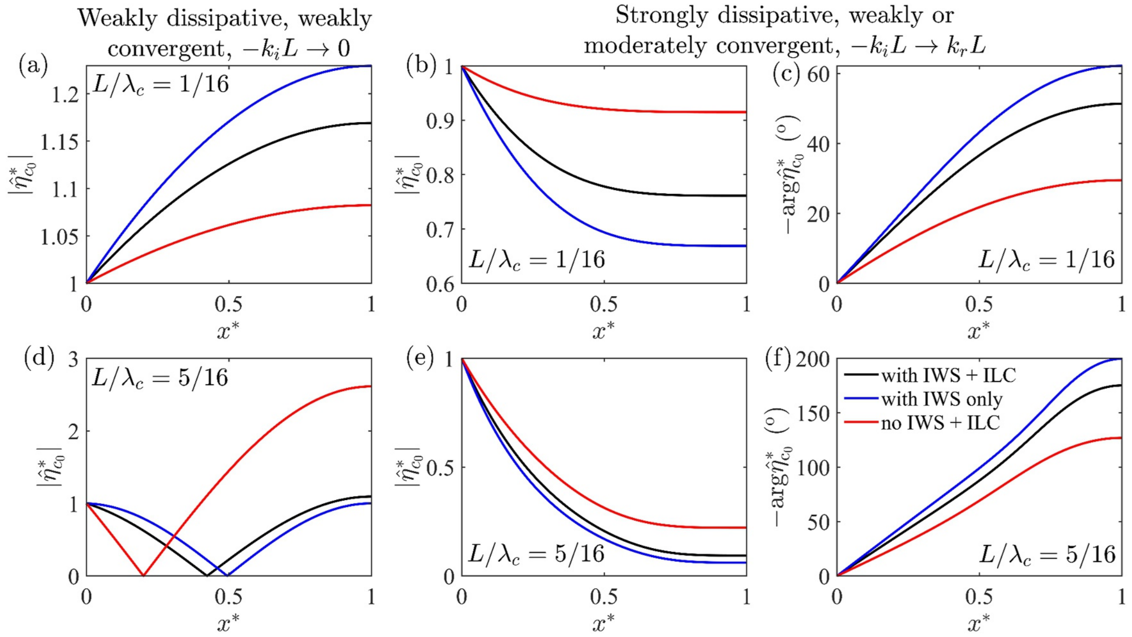

Figure 5. Along-estuary distribution of the nondimensional tidal surface amplitude in (a) a weakly dissipative and weakly convergent system with $r_B = 1.5$ and $r_H = 0.2$ and (b) a strongly dissipative, weakly or moderately convergent system with $r_B = 1.5$, $r_H = 0.2$, $s_c^* = 7$, and $s_f^* = 7$, considering $L/\lambda_c = 1/16$. (d), (e) Same as (a), (b) but for $L/\lambda_c = 5/16$. (c), (f) Same as (b), (e) but for the longitudinal patterns of the tidal phase. The black, blue, and red lines represent estuaries with intertidal zones, considering the IWS effect only, and without intertidal zones, respectively.

Therefore, within the entire parameter space (i.e., $k_rL \geq 0$ and $k_iL \leq 0$, see Table 2), intertidal zones can lead to an increase in the real and/or imaginary parts of the nondimensional wavenumber kL, while the ILC contributes to a reduction in k_rL and/or $-k_iL$, dependent on the relative importance of local inertia, estuary width convergence, and bottom friction effects. This also implies the potential shifts of the effect of intertidal areas (and its ILC contribution) across different systems. The variable ILC effects on tides and kL in different systems are summarized in Table 2, which cause an opposite contribution to the overall effects of intertidal areas.

3.2. Along-Estuary Tidal Wave Propagation

In this section, the longitudinal patterns of tidal wave propagation are further investigated in different systems as classified above. To avoid infinite tidal amplitude (i.e., resonance) which occurs at $L/\lambda_c = 1/4$ in straight frictionless estuaries (i.e., quarter-wave resonance), two different scenarios with $L/\lambda_c = 1/16$ and $5/16$ are considered, respectively corresponding to small and large wavenumber conditions. By substituting the different values of tidal wavenumber (Equations 40–45) into the analytical solution (Equation 32), the along-estuary distributions of tidal amplitude and phase can be resolved in different estuaries (as classified in Table 2) and different scenarios (i.e., with intertidal zones, considering the IWS effect only, and without intertidal zones).

In weakly dissipative and weakly convergent systems (Equation 40) with $r_B = 1.5$ and $r_H = 0.2$ (as an example), when considering a small wavenumber ($L/\lambda_c = 1/16$), the tidal amplitude increases landward along the estuary, where the overall effects of intertidal areas lead to tidal amplification but the ILC contributes to tidal damping (Figure 5a). When considering a large wavenumber ($L/\lambda_c = 5/16$), however, the tidal amplitude decreases landward to zero (i.e., resonant node) before increasing toward the estuary head (Figure 5d). Under this condition, tides at the head are attenuated by the total effects of intertidal areas but amplified by the ILC contribution, as derived in Section 3.1.1. The presence of intertidal zones also modulates the location of the resonant node (where tidal amplitude approaches zero), pushing the node further upstream (comparing black and red lines), while its ILC contribution brings the node further downstream (comparing black and blue lines in Figure 5d). The tidal phase (not shown here) in these systems remains unchanged along the estuary due to $-k_iL \to 0$, that is, standing wave with negligible damping modulus.

In strongly dissipative, weakly or moderately convergent systems (Equation 41) with $r_B = 1.5$, $r_H = 0.2$, $s_c^* = 7$, and $s_f^* = 7$ (as an example), by considering either a small or large wavenumber ($L/\lambda_c = 1/16$ or $5/16$), the tidal amplitude consistently decreases landward (Figures 5b and 5e), and the tidal phase increases landward along the estuary (Figures 5c and 5f). The decrease in the tidal surface amplitude and the increase in the phase are more significant for a larger wavenumber. The total effects of intertidal areas lead to tidal damping and phase delay (comparing black and red lines in Figures 5b–5c and 5e–5f), while the ILC makes an opposite contribution to the overall tidal changes for both small and large wavenumbers (comparing black and blue lines in Figures 5b–5c and 5e–5f), as derived in Section 3.1.2.

In weakly or moderately dissipative and strongly convergent systems, the derived tidal amplitude and phase remain unchanged along the estuary, that is, $\hat{\eta}_{c_0} = a_m$ (derived by substituting Equation 42 into Equation 32), with negligible effects of intertidal areas as explained in Section 3.1.3. In the other four intermediate systems listed in Table 2, the longitudinal patterns of tidal wave propagation lie between those of the abovementioned three specific systems, which are determined by the relative dominance of the local inertia, estuary width convergence, and bottom friction.

4. Discussion

4.1. Implications

Results in Section 3 demonstrate that the intertidal areas influence tidal propagation by modulating the complex tidal wavenumber, k, which determines the tidal properties and resonance characteristics in estuaries. The presence of intertidal areas tends to increase both the real (k_r) and imaginary ($-k_i$) parts of the wavenumber k. The ILC contribution, however, causes a reduction in both parameters, thereby partially counterbalancing the total effects of intertidal areas.

The inclusion of intertidal zones on both sides of the channel effectively decreases the mean water depth over the total cross-section. Hence, the effect of intertidal areas on tidal propagation resembles that caused by decreasing water depth (and hence decreasing λ_c), both leading to an increase in $k_r L$ and $-k_i L$. This results in a decrease in tidal wavelength or celerity and an increase in the along-estuary damping rate of both the incident and reflected waves.

The ILC effect on tidal propagation is also similar to the effect of reduced bottom friction, both reducing the tidal wavenumber (Figure 4b). This is because the along-estuary currents over intertidal areas are significant only under conditions of weak intertidal bottom friction, in contrast to the assumption of full momentum sink over intertidal areas in previous analytical models (e.g., Hepkema et al., 2018; Jay, 1991). Therefore, the ILC effect, like a reduction in estuary bottom friction, results in an increase in tidal wavelength or celerity and a decrease in damping of the incident and reflected tidal waves.

Our study yields a fundamental understanding of how intertidal areas influence estuarine tide dynamics. This offers key insights to inform the development of effective nature-based or hybrid strategies for mitigating estuarine hazards such as flooding and erosion.

4.2. Limitations

The analytical model used in this study is constrained by the specific assumptions and simplifications detailed in Section 2. For instance, the analytical solution is derived based on the assumption that the ratio of the tidal amplitude to the water depth is small ($\varepsilon \ll 1$) throughout the estuary. However, this ratio may not be small at all locations of a tidally dominated estuary, as considered here, which can bring some local deviations to model results particularly in shallow regions (J. Dronkers, 2016). Moreover, our model considers linearized bottom friction and resolves only the leading-order tidal constituent, neglecting the effects of overtides (e.g., generated by advection, density gradients, and river runoff) on the leading-order tidal motion. The linearization of bottom friction is justified by numerical and laboratory experiments with quadratic bottom friction, which produce comparable results for the dominant tide in a semi-enclosed tidal basin to those obtained with linearized bottom friction (Terra et al., 2005).

Also, by focusing on tidally dominated estuaries, we neglect the effects of river discharge on friction (Jay, 1991) and density stratification, which may reduce tidal damping (C. Zhu et al., 2021). Lateral processes in estuaries with a steep channel-shoal structure can cause tidal amplification (Ensing et al., 2015). This lateral structure, together with intertidal zones on both sides, may increase the lateral water exchange between the channel and intertidal regions and reinforce the effects of intertidal areas on tide motions in the channel (Zhou et al., 2020). However, by using the cross-sectionally averaged shallow water equations for both the intertidal and channel regions, we ignored the influence of lateral processes within both regions on the tide dynamics. Besides, by neglecting lateral variations of the water level, our model disregards the water volume deficit during flood and lagged volume during ebb in the intertidal areas relative to channel waters (Nidzieko & Ralston, 2012). Lastly, our idealized model assumes a linear intertidal bed profile (see Figure 1). In real estuaries, however, the lateral profile of intertidal bed level is either concave-up or convex-up (Friedrichs, 2011). This implies that the effects of intertidal areas might be either underestimated or overestimated due to the simplified representation of intertidal bathymetry.

5. Conclusions

In this study, we developed a one-dimensional analytical model to investigate the influence of intertidal areas on tidal wave propagation in tidally dominated estuaries, such as macro-tidal estuaries or meso-tidal estuaries during spring tides. Our model considers both the effects of the water storage (IWS) and longitudinal current (ILC) over the intertidal area. The interactions between the water motion over intertidal areas and that within the channel are dynamically resolved by computing the non-zero water exchange across the interface between the channel and intertidal zones. Our analytical solution confirms that estuarine tidal propagation is determined by two dimensionless parameters kL and L_e/L, with k the complex wavenumber, L the estuary length, and L_e the convergence length. More importantly, it reveals that intertidal zones modulate tides by influencing k through the ratio of intertidal width to the channel width (r_B) and the ratio of intertidal water flux to that in the channel (r_F), representing the IWS and ILC effects, respectively.

The effects of intertidal areas on the complex tidal wavenumber (k) and resonance characteristics were investigated, which are strongly dependent on the relative importance of local inertia, estuary width convergence, and bottom friction. The existence of intertidal areas tends to increase the real (k_r) and/or imaginary ($-k_i$) parts of the wavenumber (k). In weakly dissipative and weakly convergent estuaries ($-k_i \rightarrow 0$, dominated by local inertia), when k_rL falls below its resonance threshold, the increase in k induced by intertidal zones brings the system closer to resonance, consequently resulting in tidal amplification. Conversely, when k_rL exceeds its resonance threshold, the intertidal zone pushes the system farther from resonance, thus causing tidal damping. In strongly dissipative and weakly or moderately convergent estuaries ($k_r \rightarrow -k_i$, dominated by bottom friction), intertidal areas consistently result in tidal damping by increasing k. In weakly or moderately dissipative and strongly convergent estuaries ($k_r \rightarrow 0$, dominated by width convergence), however, tidal waves are hardly influenced by intertidal zones due to their minor effects on the wavenumber. The ILC process contributes to a reduction in k_r and/or $-k_i$, thereby partly counteracting the overall effects of intertidal areas mentioned above. This paper is Part I of a two-part series. The process associated with longitudinal currents over intertidal areas is further studied in Part II of this work.

Conflict of Interest

The authors declare no conflicts of interest relevant to this study.

Data Availability Statement

The source code for the analytical tide model and the processing code for the analytical model results used in this study are available on Zenodo (R. Zhu et al., 2025b).

Acknowledgments
This work was funded by the National Natural Science Foundation of China (NSFC, 42576156, U2040203), the Key Laboratory of Ministry of Education for Coastal Disaster and Protection, Hohai University (J202201), the Fundamental Research Funds for the Central Universities (B240205032), the China Scholarship Council (CSC, File 202406710099), and the UK Natural Environment Research Council (CHAMFER project, NE/W004992/1). This work was also supported by the Open Research Fund Program of State Key Laboratory of Water Disaster Prevention (2024491011).

References

Alebregtse, N. C., de Swart, H. E., & Schuttelaars, H. M. (2013). Resonance characteristics of tides in branching channels. *Journal of Fluid Mechanics*, *728*, R3. https://doi.org/10.1017/jfm.2013.319

Athanase, M., Sánchez-Benítez, A., Monfort, E., Jung, T., & Goessling, H. F. (2024). How climate change intensified storm Boris' extreme rainfall, revealed by near-real-time storylines. *Communications Earth & Environment*, *5*(1), 676. https://doi.org/10.1038/s43247-024-01847-0

Chernetsky, A. S., Schuttelaars, H. M., & Talke, S. A. (2010). The effect of tidal asymmetry and temporal settling lag on sediment trapping in tidal estuaries. *Ocean Dynamics*, *60*(5), 1219–1241. https://doi.org/10.1007/s10236-010-0329-8

Cundy, A. B., Lafite, R., Taylor, J. A., Hopkinson, L., Deloffre, J., Charman, R., et al. (2007). Sediment transfer and accumulation in two contrasting salt marsh/mudflat systems: The Seine Estuary (France) and the Medway Estuary (UK). *Hydrobiologia*, *588*(1), 125–134. https://doi.org/10.1007/s10750-007-0657-y

Cushman-Roisin, B., & Beckers, J. (2011). *Introduction to geophysical fluid dynamics: Physical and numerical aspects* (Vol. 101). Academic Press.

Dronkers, J. (2016). Dynamics of coastal systems. *World Scientific*.

Dronkers, J. J. (1964). *Tidal computations in rivers and coastal waters*. North-Holland Publishing Company.

Ensing, E., de Swart, H. E., & Schuttelaars, H. M. (2015). Sensitivity of tidal motion in well-mixed estuaries to cross-sectional shape, deepening, and sea level rise: An analytical study. *Ocean Dynamics*, *65*(7), 933–950. https://doi.org/10.1007/s10236-015-0844-8

Friedrichs, C. T. (2011). Estuarine sediment dynamics. In E. Wolanski, & D. McLusky (Eds.), *Treatise on estuarine and coastal science* (pp. 137–170). Academic Press.

Friedrichs, C. T., & Aubrey, D. G. (1994). Tidal propagation in strongly convergent channels. *Journal of Geophysical Research*, *99*(C2), 3321–3336. https://doi.org/10.1029/93JC03219

Friedrichs, C. T., & Madsen, O. S. (1992). Nonlinear diffusion of the tidal signal in frictionally dominated embayments. *Journal of Geophysical Research*, *97*(C4), 5637–5650. https://doi.org/10.1029/92JC00354

Green, G. (1837). On the motion of waves in a variable canal of small depth and width. *Transactions of the Cambridge Philosophical Society*. https://doi.org/10.1017/CBO9781107325074.007

Hepkema, T. M., de Swart, H. E., Zagaris, A., & Duran Matute, M. (2018). Sensitivity of tidal characteristics in double inlet systems to momentum dissipation on tidal flats: A perturbation analysis. *Ocean Dynamics*, *68*(4–5), 439–455. https://doi.org/10.1007/s10236-018-1142-z

Huang, G., Falconer, R., Lin, B., & Xu, C. (2022). Dynamic tracing of fecal bacteria processes from a river basin to an estuary using a 2D/3D model. *River*, *1*(2), 149–161. https://doi.org/10.1002/rvr2.27

Hunt, J. N. (1964). Tidal oscillations in estuaries. *Geophysical Journal of the Royal Astronomical Society*, *8*(4), 440–455. https://doi.org/10.1111/j.1365-246X.1964.tb03863.x

Jay, D. A. (1991). Green's law revisited: Tidal long-wave propagation in channels with strong topography. *Journal of Geophysical Research*, *96*(C11), 20585–20598. https://doi.org/10.1029/91JC01633

Kästner, K., Hoitink, A. J. F., Torfs, P. J. J. F., Deleersnijder, E., & Ningsih, N. S. (2019). Propagation of tides along a river with a sloping bed. *Journal of Fluid Mechanics*, *872*, 39–73. https://doi.org/10.1017/jfm.2019.331

Kim, B. G., & Cho, Y. K. (2017). Tide-induced residual circulation in a bay with laterally asymmetric depth. *Journal of Geophysical Research: Oceans*, *122*(5), 4040–4050. https://doi.org/10.1002/2016JC012473

Kumar, M., Schuttelaars, H. M., Roos, P. C., & Möller, M. (2016). Three-dimensional semi-idealized model for tidal motion in tidal estuaries. *Ocean Dynamics*, *66*(1), 99–118. https://doi.org/10.1007/s10236-015-0903-1

Lanzoni, S., & Seminara, G. (1998). On tide propagation in convergent estuaries. *Journal of Geophysical Research*, *103*(C13), 30793–30812. https://doi.org/10.1029/1998JC900015

Li, C., Schuttelaars, H. M., Roos, P. C., Damveld, J. H., Gong, W., & Hulscher, S. J. M. H. (2016). Influence of retention basins on tidal dynamics in estuaries: Application to the Ems Estuary. *Ocean & Coastal Management*, *134*, 216–225. https://doi.org/10.1016/j.ocecoaman.2016.10.010

Li, L., Wang, X. H., Williams, D., Sidhu, H., & Song, D. (2012). Numerical study of the effects of mangrove areas and tidal flats on tides: A case study of Darwin Harbour, Australia. *Journal of Geophysical Research*, *117*(C6), C06011. https://doi.org/10.1029/2011JC007494

Miles, J. W. (1971). Resonant response of harbours: An equivalent-circuit analysis. *Journal of Fluid Mechanics*, *46*(2), 241–265. https://doi.org/10.1017/S002211207100051X

Möller, I., Kudella, M., Rupprecht, F., Spencer, T., Paul, M., van Wesenbeeck, B. K., et al. (2014). Wave attenuation over coastal salt marshes under storm surge conditions. *Nature Geoscience*, *7*(10), 727–731. https://doi.org/10.1038/ngeo2251

Moraes, R. P. L., Reguero, B. G., Mazarrasa, I., Ricker, M., & Juanes, J. A. (2022). Nature-based solutions in coastal and estuarine areas of Europe. *Frontiers in Environmental Science*, *10*. https://doi.org/10.3389/fenvs.2022.829526

Murray, N. J., Phinn, S. R., Dewitt, M., Ferrari, R., Johnston, R., Lyons, M. B., et al. (2019). The global distribution and trajectory of tidal flats. *Nature*, *565*(7738), 222–225. https://doi.org/10.1038/s41586-018-0805-8

Nidzieko, N. J., & Ralston, D. K. (2012). Tidal asymmetry and velocity skew over tidal flats and shallow channels within a macrotidal river delta. *Journal of Geophysical Research*, *117*(C3), C3001. https://doi.org/10.1029/2011JC007384

Oey, L., Ezer, T., Hu, C., & Muller-Karger, F. E. (2007). Baroclinic tidal flows and inundation processes in Cook Inlet, Alaska: Numerical modeling and satellite observations. *Ocean Dynamics*, *57*(3), 205–221. https://doi.org/10.1007/s10236-007-0103-8

Rainey, R. C. T. (2009). The optimum position for a tidal power barrage in the Severn Estuary. *Journal of Fluid Mechanics*, *636*, 497–507. https://doi.org/10.1017/S0022112009991443

Ralston, D. K., Geyer, W. R., Traykovski, P. A., & Nidzieko, N. J. (2013). Effects of estuarine and fluvial processes on sediment transport over deltaic tidal flats. *Continental Shelf Research*, *60*, S40–S57. https://doi.org/10.1016/j.csr.2012.02.004

Ralston, D. K., Talke, S., Geyer, W. R., Al Zubaidi, H. A. M., & Sommerfield, C. K. (2019). Bigger tides, less flooding: Effects of dredging on barotropic dynamics in a highly modified estuary. *Journal of Geophysical Research: Oceans*, *124*(1), 196–211. https://doi.org/10.1029/2018JC014313

Roos, P. C., & Schuttelaars, H. M. (2015). Resonance properties of tidal channels with multiple retention basins: Role of adjacent sea. *Ocean Dynamics*, *65*(3), 311–324. https://doi.org/10.1007/s10236-015-0809-y

Schuttelaars, H. M., de Jonge, V. N., & Chernetsky, A. (2013). Improving the predictive power when modelling physical effects of human interventions in estuarine systems. *Ocean & Coastal Management*, *79*, 70–82. https://doi.org/10.1016/j.ocecoaman.2012.05.009

Speer, P. E., & Aubrey, D. G. (1985). A study of non-linear tidal propagation in shallow inlet/estuarine systems Part II: Theory. *Estuarine, Coastal and Shelf Science*, *21*(2), 207–224. https://doi.org/10.1016/0272-7714(85)90097-6

Stark, J., Smolders, S., Meire, P., & Temmerman, S. (2017). Impact of intertidal area characteristics on estuarine tidal hydrodynamics: A modelling study for the Scheldt Estuary. *Estuarine, Coastal and Shelf Science*, *198*, 138–155. https://doi.org/10.1016/j.ecss.2017.09.004

Talke, S. A., & Jay, D. A. (2020). Changing tides: The role of natural and anthropogenic factors. *Annual Review of Marine Science*, *12*(1), 121–151. https://doi.org/10.1146/annurev-marine-010419-010727

Terra, G. M., van de Berg, W. J., & Maas, L. R. M. (2005). Experimental verification of Lorentz' linearization procedure for quadratic friction. *Fluid Dynamics Research*, *36*(3), 175–188. https://doi.org/10.1016/j.fluiddyn.2005.01.005

Townend, I., & Whitehead, P. (2003). A preliminary net sediment budget for the Humber Estuary. *Science of the Total Environment*, *314–316*, 755–767. https://doi.org/10.1016/s0048-9697(03)00082-2

van der Wal, D., Pye, K., & Neal, A. (2002). Long-term morphological change in the Ribble Estuary, Northwest England. *Marine Geology*, *189*(3–4), 249–266. https://doi.org/10.1016/S0025-3227(02)00476-0

Verney, R., Brun-Cottan, J., Lafite, R., Deloffre, J., & Taylor, J. A. (2006). Tidally-induced shear stress variability above intertidal mudflats. Case of the macrotidal Seine Estuary. *Estuaries and Coasts*, *29*(4), 653–664. https://doi.org/10.1007/BF02784290

Winant, C. D. (2007). Three-dimensional tidal flow in an elongated, rotating basin. *Journal of Physical Oceanography*, *37*(9), 2345–2362. https://doi.org/10.1175/JPO3122.1

Winterwerp, J. C., & Wang, Z. B. (2013). Man-induced regime shifts in small estuaries—I: Theory. *Ocean Dynamics*, *63*(11–12), 1279–1292. https://doi.org/10.1007/s10236-013-0662-9

Winterwerp, J. C., Wang, Z. B., van Braeckel, A., van Holland, G., & Kösters, F. (2013). Man-induced regime shifts in small estuaries—II: A comparison of rivers. *Ocean Dynamics*, *63*(11–12), 1293–1306. https://doi.org/10.1007/s10236-013-0663-8

Wood, R. G., Black, K. S., Jago, C. F., Black, K. S., Paterson, D. M., & Cramp, A. (1998). Measurements and preliminary modelling of current velocity over an intertidal mudflat, Humber Estuary, UK. *Geological Society Special Publications*, *139*(1), 167–175. https://doi.org/10.1144/GSL.SP.1998.139.01.13

Zheng, L., Chen, C., & Liu, H. (2003). A modeling study of the Satilla River Estuary, Georgia. I: Flooding-drying process and water exchange over the salt marsh-estuary-shelf complex. *Estuaries*, *26*(3), 651–669. https://doi.org/10.1007/BF02711977

Zhou, J., Stacey, M. T., Holleman, R. C., Nuss, E., & Senn, D. B. (2020). Numerical investigation of baroclinic channel-shoal interaction in partially stratified estuaries. *Journal of Geophysical Research: Oceans*, *125*(4), e2020JC016135. https://doi.org/10.1029/2020JC016135

Zhu, C., van Maren, D. S., Guo, L., Lin, J., He, Q., & Wang, Z. B. (2021). Effects of sediment-induced density gradients on the estuarine turbidity maximum in the Yangtze Estuary. *Journal of Geophysical Research: Oceans*, *126*(5), e2020JC016927. https://doi.org/10.1029/2020JC016927

Zhu, R., Zhang, W., & Wei, X. (2025a). Impact of intertidal habitats on hydrodynamics in tidally energetic, well-mixed estuaries. *Journal of Physical Oceanography*, *55*(8), 1155–1191. https://doi.org/10.1175/JPO-D-23-0172.1

Zhu, R., Zhang, W., & Wei, X. (2025b). Model code used in the study "Impact of intertidal areas on tidal propagation in tidally dominated estuaries" [Software]. *Zenodo*. https://doi.org/10.5281/zenodo.17477388